



Article

Structure and Photoluminescence of WO_{3-x} Aggregates Tuned by Surfactants

Biben Wang ¹, Xiaoxia Zhong ^{2,*}, Haiyan Xu ³, Yongcai Zhang ⁴, Uros Cvelbar ⁵ and Kostya (Ken) Ostrikov ^{6,7}

¹ College of Chemistry and Chemical Engineering, Chongqing University of Technology, 69 Hongguang Rd, Lijiatuo, Banan District, Chongqing 400054, China

² State Key Laboratory of Advanced Optical Communication and Networks, Key Laboratory for Laser Plasmas (Ministry of Education), School of Physics and Astronomy, Shanghai Jiao Tong University, Shanghai 200240, China

³ School of Materials and Chemical Engineering, Anhui Jianzhu University, Hefei 230601, China

⁴ School of Chemistry and Chemical Engineering, Yangzhou University, Yangzhou 225009, China

⁵ Jozef Stefan Institute, Jamova Cesta 39, SI-1000 Ljubljana, Slovenia

⁶ School of Chemistry and Physics, Queensland University of Technology, Brisbane, QLD 4000, Australia

⁷ Centre for Materials Science, Queensland University of Technology, Brisbane, QLD 4000, Australia

* Correspondence: xxzhong@sjtu.edu.cn

Abstract: The optoelectronic properties of transition metal oxide semiconductors depend on their oxygen vacancies, nanostructures and aggregation states. Here, we report the synthesis and photoluminescence (PL) properties of substoichiometric tungsten oxide (WO_{3-x}) aggregates with the nanorods, nanoflakes, submicro-spherical-like, submicro-spherical and micro-spherical structures in the acetic acid solution without and with the special surfactants (butyric or oleic acids). Based on theory on the osmotic potential of polymers, we demonstrate the structural change of the WO_{3-x} aggregates, which is related to the change of steric repulsion caused by the surfactant layers, adsorption and deformation of the surfactant molecules on the WO_{3-x} nanocrystals. The WO_{3-x} aggregates generate multi-color light, including ultraviolet, blue, green, red and near-infrared light caused by the inter-band transition and defect level-specific transition as well as the relaxation of polarons. Compared to the nanorod and nanoflake WO_{3-x} aggregates, the PL quenching of the submicro-spherical-like, submicro-spherical and micro-spherical WO_{3-x} aggregates is associated with the coupling between the WO_{3-x} nanoparticles and the trapping centers arising from the surfactant molecules adsorbed on the WO_{3-x} nanoparticles.

Keywords: WO_{3-x} nanocrystals; steric repulsion; aggregation; surfactants; photoluminescence



Citation: Wang, B.; Zhong, X.; Xu, H.; Zhang, Y.; Cvelbar, U.; Ostrikov, K. Structure and Photoluminescence of WO_{3-x} Aggregates Tuned by Surfactants. *Micromachines* **2022**, *13*, 2075. <https://doi.org/10.3390/mi13122075>

Academic Editors: Elham Gharibshahi and Miltiadis (Miltos) Alamaniotis

Received: 31 October 2022

Accepted: 23 November 2022

Published: 25 November 2022

Publisher's Note: MDPI stays neutral with regard to jurisdictional claims in published maps and institutional affiliations.



Copyright: © 2022 by the authors. Licensee MDPI, Basel, Switzerland. This article is an open access article distributed under the terms and conditions of the Creative Commons Attribution (CC BY) license (<https://creativecommons.org/licenses/by/4.0/>).

1. Introduction

Tungsten oxides are important semiconductor materials. Since their excellent physical and chemical properties are linked to the size, oxygen vacancies, nanostructures and aggregation states, it is still a significant challenge to tune their structures and properties [1,2]. When inorganic nanomaterials are synthesized in solutions, surfactants are universally used to tune their structures by adjusting the aggregation of nanocrystals [3–6]. For example, the In_2O_3 nanodots are aggregated into nanoflowers depending on myristic acid [6]. Furthermore, the studies indicate that some properties of the aggregated materials (e.g., carrier transport and photoluminescence) strongly depend on the coupling separation between the nanocrystals [5,7], which are related to the lengths of the surfactant molecules [8–10]. In other words, surfactants play important roles in tuning the aggregated nanomaterials' structures and properties. In a solution containing the surfactants, there are attraction and repulsive interactions between the nanocrystals. The attraction interactions (i.e., dipole-dipole and van der Waals interactions) promote the aggregation between the nanocrystals, while the repulsive interactions (e.g., steric and electrostatic repulsion forces)

hinder the aggregation [3,11]. Due to the strong attraction interactions, the nanocrystals are aggregated together [11]. Therefore, tuning of the aggregation process weakens the attractions by the introduction of the surfactants. This paper explores the tuning of the structures and photoluminescence (PL) properties of substoichiometric tungsten oxide (WO_{3-x} , $2 < x < 3$) aggregates through adjusting the aggregation process using the solvothermal synthesis technique.

Compared to stoichiometric tungsten oxides (WO_3 and WO_2), the WO_{3-x} nanomaterials have fascinating luminescent and catalytic properties, which are related to the aggregation and the defect levels formed by the oxygen vacancies [12–17]. In other words, the WO_{3-x} materials are becoming the important semiconductor materials for optoelectronic and catalytic applications. Therefore, the WO_{3-x} materials have attracted considerable attention and great efforts contribute to the foundation and application studies in recent years [14,15,17–21].

Various WO_{3-x} nanostructures (e.g., films, nanowires, nanodots and hybrid nanostructures) have been fabricated using physical and chemical methods [12,14,19–21]. In particular, the WO_{3-x} nanomaterials are universally synthesized in different solvents using the solvothermal method [22]. It is well known that various WO_{3-x} nanostructures are made up of nanoparticles, i.e., the WO_{3-x} nanostructures can be tuned by adjusting the aggregation of the WO_{3-x} nanoparticles. The early studies indicate that the aggregation of the WO_{3-x} nanoparticles is indeed tuned by the surfactants [23,24]. However, the mechanism has not been well understood because the repulsion effects caused by the surfactants involve the lengths, adsorption, compress, etc. of the surfactant molecules [25]. In this paper, the special surfactants (i.e., butyric acid and oleic acid) were employed to tune the structures of the WO_{3-x} aggregates, respectively. Based on the osmotic potential of polymers, the effects of the surfactants on the aggregation of the WO_{3-x} nanoparticles are analyzed. Furthermore, the PL properties of the WO_{3-x} aggregates were studied.

2. Materials and Method

2.1. Materials

In the process of synthesizing the WO_{3-x} aggregates, the WCl_6 powder, acetic, butyric and oleic acids were used as the precursors. Among these precursors, the WCl_6 powder (99%) was supplied by Yanyu (Shanghai) Chemical Agent Co., Ltd.) and all the carboxylic acids including acetic acid ($\geq 99.8\%$), butyric acid (99%) and oleic acid (chemical grade) were provided by Shanghai Macklin Biochemical Technology Co., Ltd. (Shanghai, China). The previous studies indicate that the metal acetate was used to fabricate the corresponding metal oxide nanocrystals [6]. Here, the WCl_6 powder and acetic acid was used to synthesize the WO_{3-x} nanocrystals, and the butyric and oleic acids were used as the surfactants to tune the structure of the WO_{3-x} aggregates, respectively.

2.2. Synthesis

Due to differences in the viscosity of different carboxylic acids, the acetic acid and surfactant were mixed in a 100 mL Teflon-lined autoclave by magnetic stirring for 30 min to ensure the uniformity of the solution. After the WCl_6 powder was poured into the solution, the solution was further stirred magnetically for 30 min, and then the autoclave was encapsulated in a stainless tank. In a heating furnace, the tank was heated to $120\text{ }^\circ\text{C}$ in ~ 60 min and maintained for 12 h at this temperature. The loose WO_{3-x} agglomerate was obtained at room temperature by centrifugal precipitation and drying treatment for 12 h at $50\text{ }^\circ\text{C}$. Furthermore, the agglomerate was ground into the powder to use for further characterizations. Different WO_{3-x} samples were synthesized in the experiments and the synthesis conditions are summarized in Table 1.

Table 1. Mass of WCl_6 , volume of carboxylic acids, growth temperature (T), and time (t).

Sample	WCl_6 (g)	Acetic Acid (mL)	Butyric Acid (mL)	Oleic Acid (mL)	T ($^{\circ}C$)	t (h)
A	2.00	50	-	-	120	12
B	2.00	30	20	-	120	12
C	2.00	20	30	-	120	12
D	2.00	30	-	20	120	12
E	2.00	20	-	30	120	12

2.3. Characterization and PL Measurement

The phases and composition of the as-synthesized WO_{3-x} aggregates are determined according to the data recorded in a TTRAX3 X-ray diffractometer (XRD) using a $Cu K\alpha$ radiation with a wavelength of 0.154 nm and a Horiba Scientific LabRAM HR evolution Raman spectrometer under irradiation of the 532 nm line of a semiconductor laser, respectively. The binding states of elements were analyzed depending on the data obtained from an ESCALAB 250 X-ray photoelectron spectroscopy (XPS) equipped with an Al $K\alpha$ X-ray source. The studies on the surface morphology and microstructures were carried out in an S-4800 field emission scanning electron microscope (FESEM) (operated at 5 kV) and a TECNAI G² F30 high-resolution transmission electron microscope (TEM) (operated at 300 kV), respectively.

At room temperature, the PL emission from the as-synthesized aggregates was measured in the Horiba Scientific LabRAM HR evolution Raman spectrometer under irradiation of the He-Cd laser with a wave length of 325 nm and $\sim 1 \mu m$ diameter of laser beam. During the PL measurement, the power of laser and the acquisition time were set to 6.8 mW and 30 s, respectively.

3. Results

3.1. Phases and Composition

The phases and composition of the as-synthesized WO_{3-x} aggregates are determined by the XRD and Raman results. The XRD patterns of samples A–D are presented in Figure 1 and the phases corresponding to the peaks are summarized in Table 2. According to the data in Table 2, the as-synthesized materials are the WO_{3-x} materials composed of the $W_{19}O_{55}$, $WO_{2.92}$ and $W_{18}O_{49}$ phases. Furthermore, Figure 1 indicates that the strongest peaks in Figure 1b become wide compared to the strongest peak in Figure 1a. In other words, the size of WO_{3-x} nanoparticles synthesized in the solution containing the surfactant becomes small.

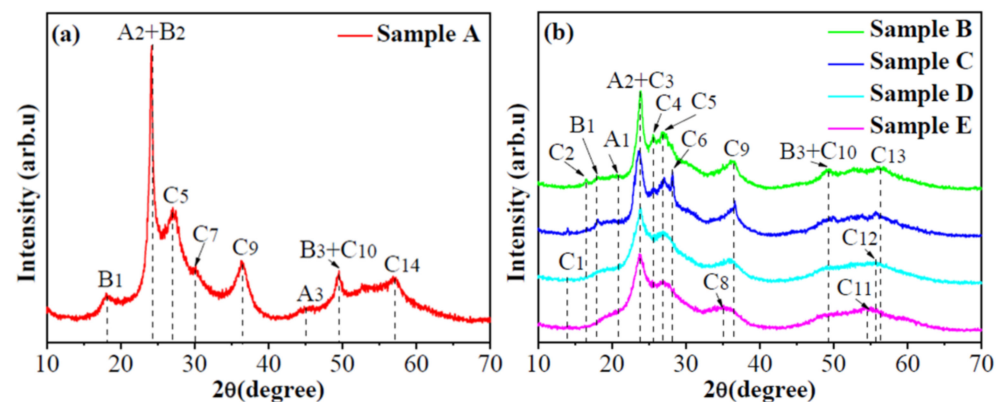
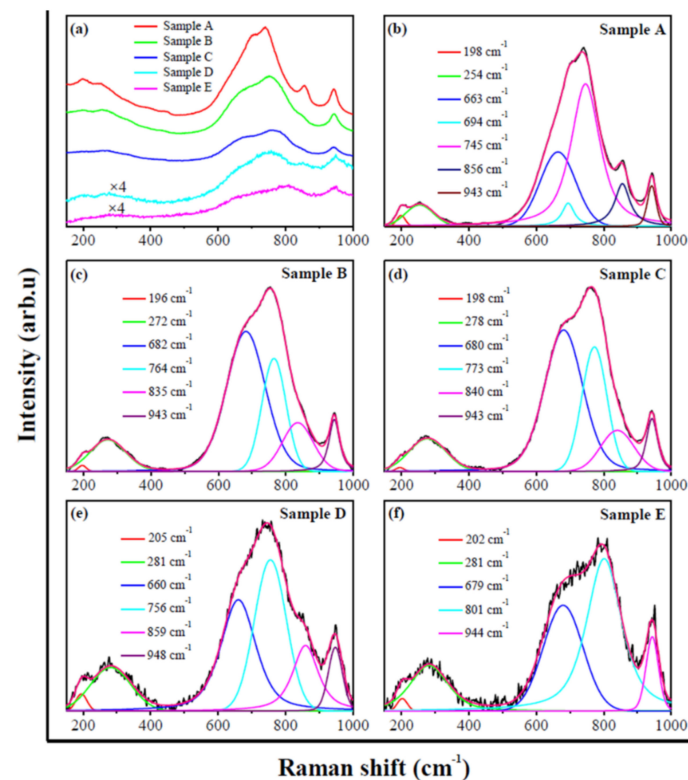


Figure 1. XRD patterns of as-synthesized WO_{3-x} aggregates of (a) sample A and (b) samples B–E respectively, which indicate that they are composed of mixed phases.

Table 2. Phases responding to the XRD peaks in Figure 1a,b.

Phase	Peak	JCPDS
A ₁ : W ₁₉ O ₅₅ (-105); A ₂ : W ₁₉ O ₅₅ (302); A ₃ : W ₁₉ O ₅₅ (-2011)	20.5°, 24.0°, 45.9°	45-0167
B ₁ : WO _{2.92} (-1012); B ₂ : WO _{2.92} (-1016); B ₃ : WO _{2.92} (-2128)	18.5°, 24.0°, 49.8°	30-1387
C ₁ : W ₁₈ O ₄₉ (-301); C ₂ : W ₁₈ O ₄₉ (102); C ₃ : W ₁₈ O ₄₉ (103)	14.5°, 16.6°, 24.0°	05-0392
C ₄ : W ₁₈ O ₄₉ (302); C ₅ : W ₁₈ O ₄₉ (012); C ₆ : W ₁₈ O ₄₉ (211)	25.6°, 27.4°, 28.1°	
C ₇ : W ₁₈ O ₄₉ (501); C ₈ : W ₁₈ O ₄₉ (502); C ₉ : W ₁₈ O ₄₉ (-704)	30.6°, 35.8°, 36.6°	
C ₁₀ : W ₁₈ O ₄₉ (021); C ₁₁ : W ₁₈ O ₄₉ (123); C ₁₂ : W ₁₈ O ₄₉ (-523)	49.8°, 54.4°, 55.7°	
C ₁₃ : W ₁₈ O ₄₉ (017); C ₁₄ : W ₁₈ O ₄₉ (-1015)	56.3°, 57.3°	

The Raman spectra presented in Figure 2 further evidence that the as-synthesized materials are the WO_{3-x} aggregates. To clearly distinguish the Raman peaks, the Raman spectra in Figure 2a are deconvoluted and the results are presented in Figure 2b–f. In Table 3, the deconvoluted Raman peaks are assigned and summarized. Depending on the studies [26], the Raman peaks at 835–859 cm⁻¹ may result from the vibration modes of different W–O bonds.

**Figure 2.** Raman spectra (a) and deconvoluted Raman spectra (b–f) of as-synthesized WO_{3-x} aggregates. The data in the insets are the positions corresponding to Raman peaks.**Table 3.** Assignment of Raman peaks in Figure 2.

Raman Peak (cm ⁻¹)	Assignment *	References
196, 198	Lattice vibration	[26]
205, 254	ν (W–O–W)	[27]
272, 278, 281	δ (O–W–O)	[27,28]
660, 663, 679, 680, 682, 694	ν (O–W–O)	[27]
745, 756, 764, 773	ν (W–O)	[13,28]
801	ν (O–W–O)	[28]
943, 944, 948	ν (W=O)	[13,28]

* δ and ν represent the bending and stretching vibration modes, respectively.

Furthermore, the Raman peaks in a range of 200–400 cm^{-1} are associated with the vibration of $\text{W}^{5+}-\text{O}$ bonds, which indicate the formation of the WO_{3-x} aggregates [29]. In addition, the studies indicate that the Raman spectrum of pure WO_3 shows the sharp characteristic peaks at about 806, 716, 326 and 272 cm^{-1} , while the spectra of WO_{3-x} exhibit the wide peaks at these positions and some new peaks due to the distortions in the crystalline structure [30]. According to the studies [30], the Raman peaks in Figure 2 further address that the as-synthesized materials are the WO_{3-x} aggregates.

3.2. Binding States of Elements

The XPS spectra are usually used to analyze the binding states of elements. The XPS survey spectra presented in Figure 3 indicate that the as-synthesized aggregates contain the W, O and C elements. In order to confirm the binding states of these elements, a XPSPEAK 41 analysis software was used to deconvolute the W 4f, O 1s and C 1s XPS spectra after Shirley background subtraction. The results are presented in Figure 4 and the deconvoluted peaks are summarized in Table 4.

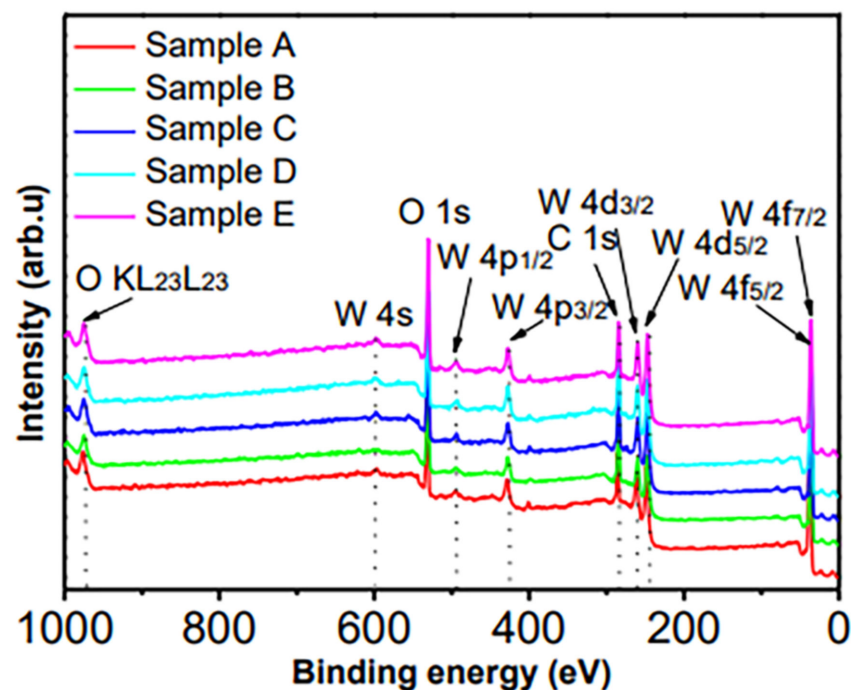


Figure 3. XPS survey spectra of samples A–D. The XPS peaks are assigned according to Ref. [31]. These XPS peaks indicate that the as-synthesized aggregates contain the W, O and C elements.

Table 4. Binding energy (eV) of deconvoluted XPS peaks in Figure 4.

Sample	$\text{W}^{5+} 4f_{7/2}$	$\text{W}^{6+} 4f_{7/2}$	$\text{W}^{5+} 4f_{5/2}$	$\text{W}^{6+} 4f_{5/2}$	O_L	O_V	O_C	$(\text{CH}_2)_n$	CH_2O	$\text{O}=\text{C}-\text{O}$
A	34.7	35.5	36.1	37.8	530.4	531.5	532.8	284.7	285.8	289.0
B	34.8	35.6	36.3	37.8	530.4	531.7	533.1	284.7	285.6	288.9
C	34.7	35.6	36.3	37.8	530.4	531.7	533.1	284.7	285.5	288.9
D	34.9	35.6	36.2	37.8	530.5	531.7	533.0	284.7	285.6	288.9
E	34.7	35.6	36.2	37.8	530.3	531.3	532.7	284.7	285.5	288.9

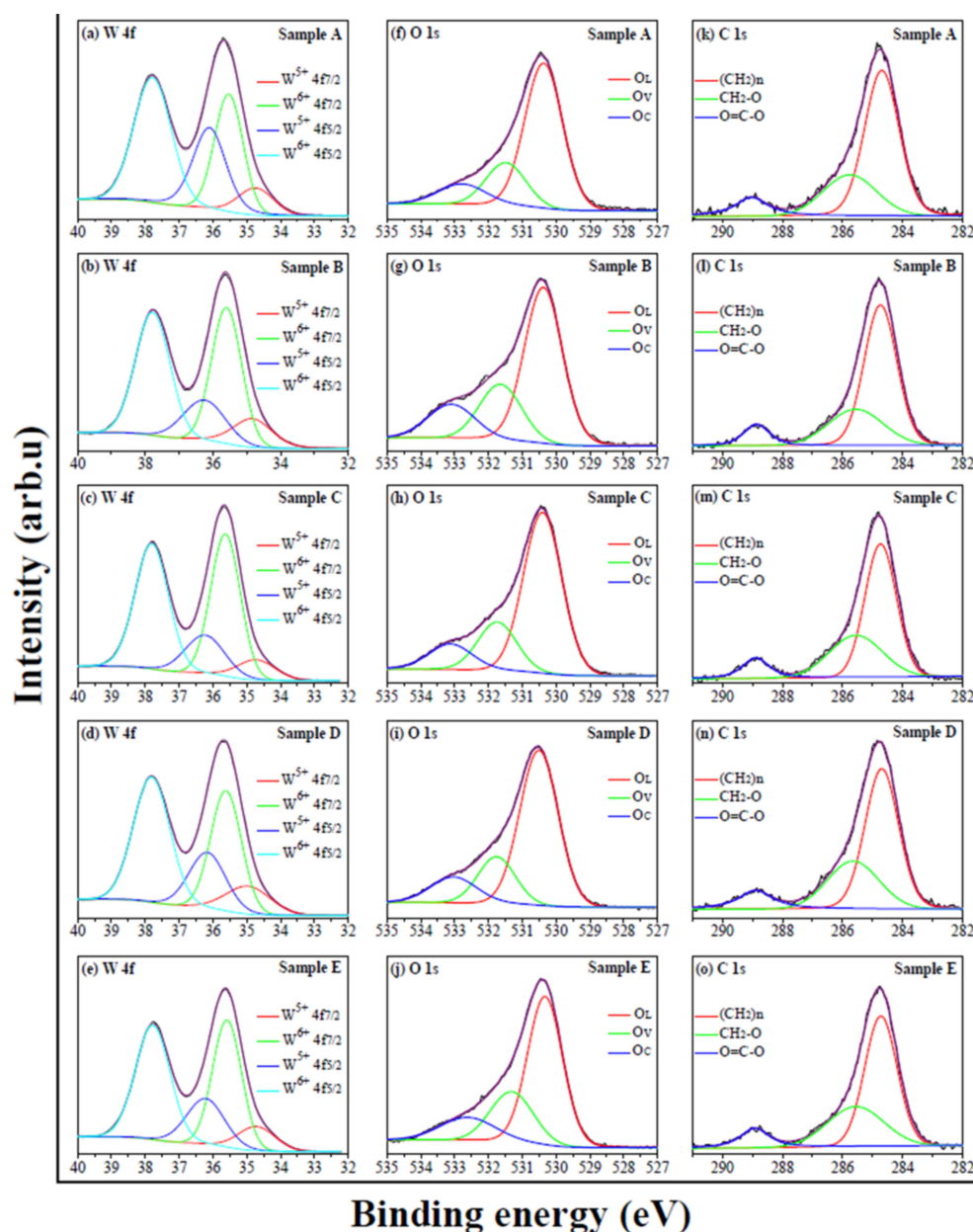


Figure 4. High-resolution W 4f, O 1s and C 1s XPS spectra of as-synthesized WO_{3-x} aggregates. The deconvoluted peaks indicate the presence of oxygen vacancies and the absorption of carboxylic acid molecules.

From Figure 4a–d, one can see that the W 4f XPS spectra feature two pair of peaks, i.e., one pair of peaks at about 34.7–34.9 eV and 36.1–36.3 eV are attributed to $\text{W}^{5+} 4f_{7/2}$ and $\text{W}^{5+} 4f_{5/2}$, and another pair at about 35.5–35.6 eV and 37.8 eV correspond to $\text{W}^{6+} 4f_{7/2}$ and $\text{W}^{6+} 4f_{5/2}$ [32,33]. The O 1s XPS spectra in Figure 4f–j are deconvoluted into three peaks located at about 530.3–530.5, 531.3–531.7 and 532.7–533.1 eV, which are related to the oxygen atoms in the lattices (O_L), the oxygen in the vicinity of oxygen vacancies (O_V) and the oxygen atoms of carboxylic groups (O_C) [32,34], respectively. Similarly, the C 1s XPS spectra in Figure 4k–o are fitted by three peaks at about 284.7, 285.5–285.8 and 288.9–289.0 eV, and they are attributed to $(\text{CH}_2)_n$, $\text{CH}_2\text{-O}$ and $\text{O}=\text{C}-\text{O}$ [31,34], respectively.

The appearance of the XPS peaks related to W^{5+} indicates the formation of the WO_{3-x} structure and the creation of oxygen vacancies [16]. Furthermore, the O 1s XPS spectra confirm the presence of oxygen vacancies, and the carboxyl acid molecules are adsorbed on

the surfaces of the WO_{3-x} aggregates and they are bonded on the surface in the bidentate interaction modes [35].

According to Figure 4f–j, the areas of O_L , O_V and O_C peaks are obtained and they are summarized in Table 5. Referring to Ref. [36], the coverage ratios of the oxygen vacancies on the sample surfaces (i.e., the area ratio R of O_V peak to the area sum of O_L and O_V peaks) are calculated and the results are shown in Table 5. The studies indicate that the insulativity of metal oxides is enhanced by the reduction of oxygen vacancies [37]. In other words, the conductivity is enhanced by the oxygen vacancies. Based on the relation of the conductivity with the oxygen vacancies, the data in Table 5 indicate that the conductivity of sample B is high compared to sample A. Furthermore, the conductivity of samples C and D reduces compared to sample B. However, the conductivity of sample E becomes higher than sample B. The change in the conductivity may originate from the structural conversion of the WO_{3-x} aggregates and the amount of carboxylic acid as well as the lengths of carboxylic acid molecules. The SEM images (see Figure 5) indicate that the structures of samples A and B convert from the nanorods and nanoflakes to the aggregates of the nanoparticles. As a result, the surface area of sample B is enhanced to increase the oxygen vacancies. Compared to sample B, Table 1 indicates that the amount of butyric acid increases for sample C, which implies that more butyric acid molecules adsorb on the surface of the WO_{3-x} nanoparticles to increase the insulativity. Therefore, the conductivity is reduced. When sample D was synthesized, oleic acid was employed. Due to the long chain of an oleic acid molecule, the insulativity of sample D is enhanced to reduce the conductivity. For sample E, much oleic acid was used. The high viscosity of oleic acid leads to the reduction of the oleic acid molecules adsorbed on the WO_{3-x} nanoparticles (see the analyses in Section 3.4). As a consequence, the conductivity is increased.

Table 5. Areas of O_L , O_V and O_C peaks and the area ratio R of O_V peak to the area sum of O_L and O_V peaks.

Sample	O_L Peak Area	O_V Peak Area	O_C Peak Area	Ratio (%)
A	50,970	17,025	11,230	25.0
B	39,685	16,637	12,062	29.5
C	52,013	17,025	10,649	24.7
D	54,684	16,901	11,866	23.6
E	47,576	20,926	14,301	30.5

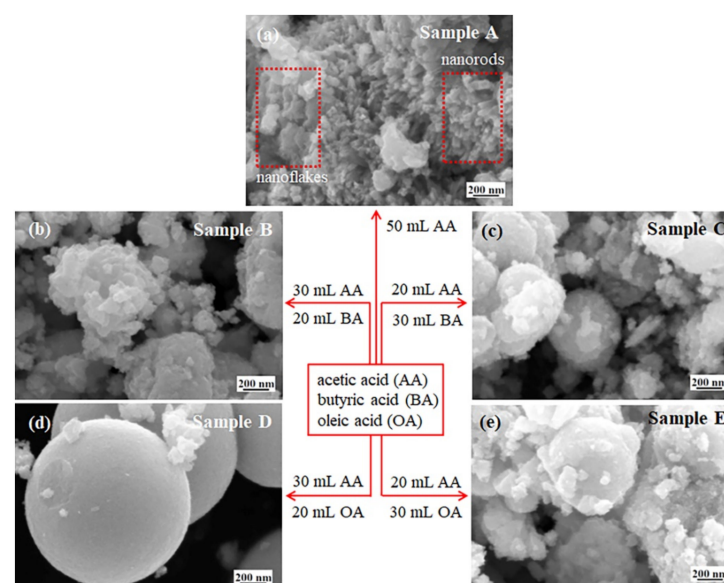


Figure 5. FESEM images of samples A–E. These images indicate that the as-synthesized WO_{3-x} materials are the mixture of (a) nanoflakes and aggregated nanodots, (b,e) the submicro-spherical-like, (c) submicro-spherical and (d) micro-spherical structures mixed with the aggregated nanoparticles.

3.3. Morphology and Microstructure

The morphologies of the as-synthesized WO_{3-x} aggregates are presented in Figure 5. Figure 5a exhibits that sample A contains the nanoflakes and nanorods as well as some aggregated nanoparticles, which indicate that the WO_{3-x} nanoparticles are aggregated in an oriented mode in acetic acid solution.

Figure 5b–e exhibit the mixture of the submicro-spherical-like, submicro-spherical and micro-spherical structures mixed with the aggregated nanoparticles, respectively. These indicate that the aggregation of the WO_{3-x} nanoparticles is changed by the butyric acid or oleic acid, i.e., they are aggregated in a disoriented mode, but the aggregation is related to the amount of the surfactants. From Figure 5b–e, one can see that the increase in the amount of butyric acid leads to the structural conversion from submicro-spherical-like to submicro-spherical shapes, while the enhancement of oleic acid results in the change from micro-spherical to submicro-spherical-like shapes.

The microstructures of samples A, B and D are revealed in Figures 6–8. The high-resolution TEM images presented in Figure 6 indicate that the nanoflake, nanorod and nanoparticle in sample A are well crystallized. After the thickness of five crystal planes are measured using digital micrograph software, the lattice distances of the nanoflake, nanorod and nanoparticle are obtained. They are ~ 0.376 , 0.369 and 0.383 nm, respectively, which correspond to the d values (0.368 and 0.370 nm) of the $\text{WO}_{2.92}(-1016)$ and $\text{W}_{19}\text{O}_{55}(302)$ [JCPDS: 30-1387 and 45-0167].

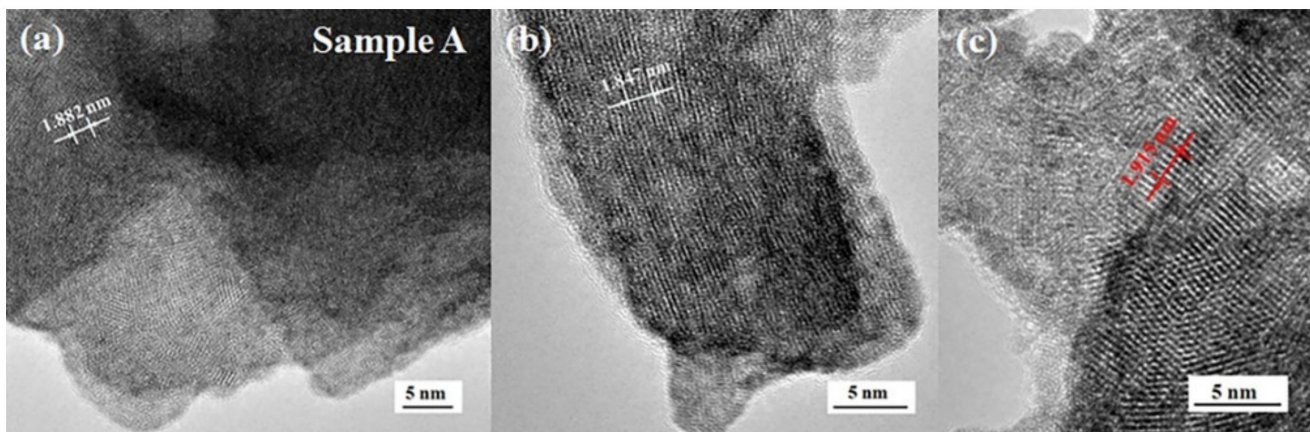


Figure 6. TEM images of sample A, which indicate that the nanoflake (a), nanorod (b) and nanoparticle (c) are the crystal structure with the lattice spacing of ~ 0.376 , 0.369 and 0.383 nm, respectively.

The TEM images in Figure 7 indicate that the WO_{3-x} aggregates in sample B are the submicro-spherical-like structure mixed with some nanorods. Similar to Figure 6, the thickness of ten or five crystal planes are measured using digital micrograph software. According to the thickness values, the lattice spacing of the nanorod and nanoparticle are, respectively, ~ 0.378 and 0.380 nm, which correspond to the d values (0.370 and 0.373 nm) of the $\text{W}_{19}\text{O}_{55}(302)$ and $\text{W}_{18}\text{O}_{49}(103)$ [JCPDS: 45-0167 and 05-0392].

The TEM images of sample D presented in Figure 8 exhibit a micro-spherical structure. According to the measured thickness of five crystal planes, the lattice spacing is about 0.389 nm, which corresponds to the d value (0.373 nm) of $\text{W}_{18}\text{O}_{49}(103)$ [JCPDS: 05-0392].

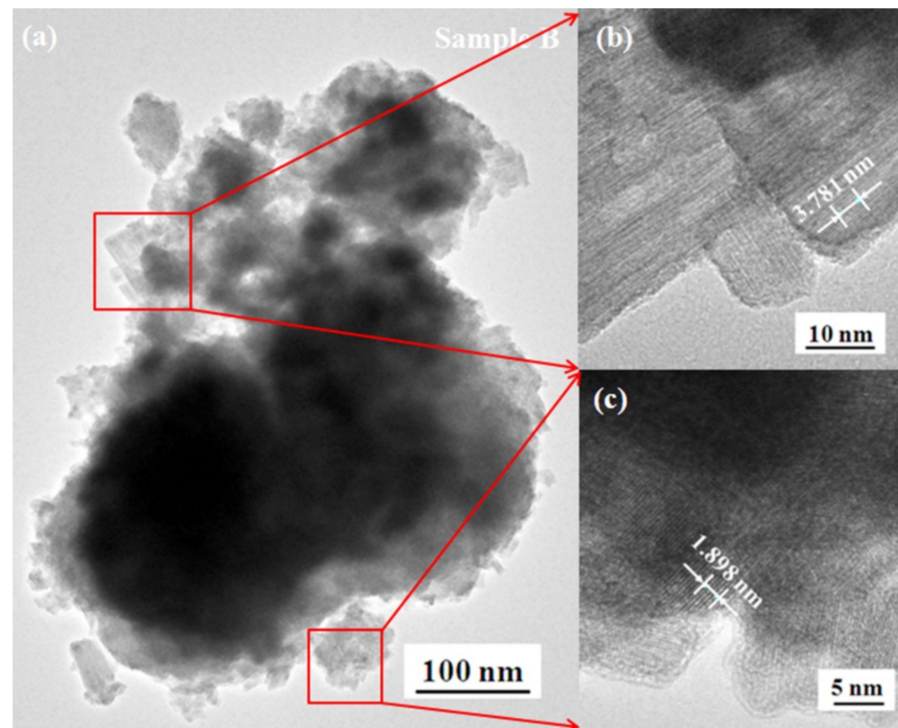


Figure 7. TEM images of sample B. The image (a) indicates that sample B is the submicro-spherical-like structure mixed some nanorods and the submicro-spherical-like structure is aggregated by nanoparticles. The high-resolution TEM images indicate that the nanorod (b) and nanoparticle (c) are the crystalline structure with the lattice spacing of ~ 0.378 and 0.380 nm, respectively.

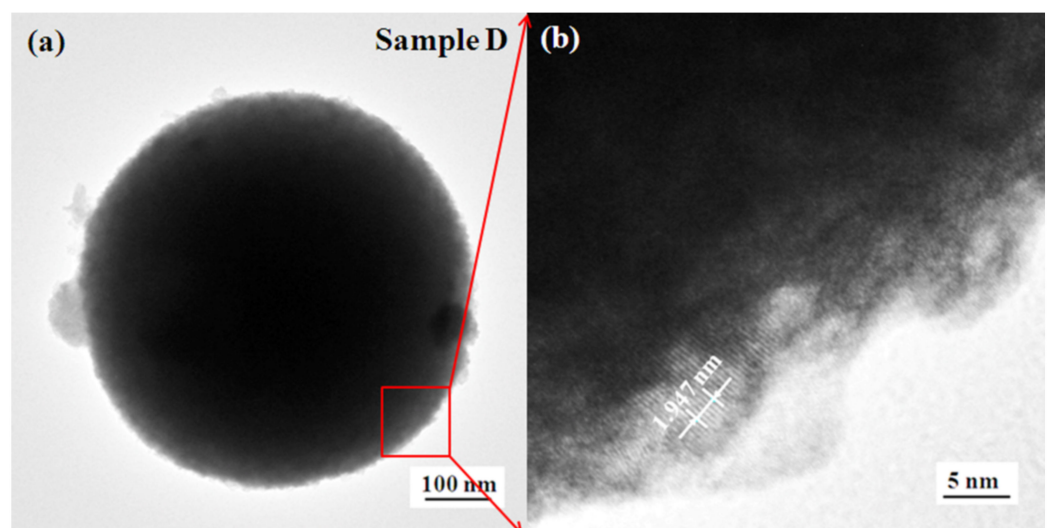


Figure 8. TEM images of sample D. Image (a) indicates that the edge is composed of nanoparticles. The high-resolution TEM image (b) indicates that the nanoparticle is the crystalline structure with a lattice spacing of ~ 0.389 nm.

3.4. Aggregation of WO_{3-x} Nanoparticles in Different Solutions

3.4.1. Aggregation of WO_{3-x} Nanoparticles in Acetic Acid

In an earlier paper [13], the formation of the WO_{3-x} nanoparticles in acetic acid was studied, which involves the $WCl_6-CH_3CO_2H$ reaction and the condensation reaction. The $WCl_6-CH_3CO_2H$ reaction leads to the formation of tungsten acetate, and the further condensation reaction of tungsten acetate forms the WO_{3-x} nanoparticles. In acetic acid solution, the WO_{3-x} nanoparticles are covered by the acetic acid molecules. As a result, the

WO_{3-x} nanoparticles experience a quenching for a long time to form the WO_{3-x} nanocrystals (NCs). The XPS results indicate the adsorption of the acetic acid molecules on the surfaces of the WO_{3-x} NCs, which indicates that a protecting layer is formed to prevent the aggregation of the WO_{3-x} NCs [38]. However, the adsorption is reversible due to the low molecular weight of acetic acid [25,39]. In other words, some acetic acid molecules can be desorbed from the WO_{3-x} NCs. Due to the anisotropy of the WO_{3-x} NCs, the acetic acid molecules coordinated with the tungsten atoms are changed to selectively adsorb on the special crystal planes [40]. As a result, a strong dipole–dipole interaction occurs between the WO_{3-x} NCs. The directionality of the dipole–dipole interaction leads to the aggregation of the WO_{3-x} NCs along a direction to form the nanorods [11]. As for the formation of the WO_{3-x} nanoflakes, it is related to the gas-liquid interface formed by acetic acid. Due to Brownian motion, some WO_{3-x} NCs move to the gas-liquid interface. Some acetic acid molecules adsorbed on the upper and side surfaces of the WO_{3-x} NCs on the interface are desorbed. As a result, the strong dipole–dipole interaction between the WO_{3-x} NPs leads to the aggregation [11]. During the aggregation, the WO_{3-x} NCs are still constrained on the interface. Finally, the aggregation results in the formation of the WO_{3-x} nanoflakes.

3.4.2. Aggregation under Surfactants

After the surfactant (i.e., butyric acid or oleic acid) is added, it leads to the WO_{3-x} nanoparticles' size, motion and distribution changes. At the same time, the addition of the surfactant results in the change of the viscosity of the solution. These changes further cause the change in the aggregation process of the WO_{3-x} nanoparticles.

1. Changes in size, motion and distribution of WO_{3-x} nanoparticles

In the nucleation process, the surfactant molecules are adsorbed on the surfaces of the WO_{3-x} nuclei. Unlike the acetic acid molecules, the surfactant molecules have a high molecular weight, which lead to a relatively irreversible adsorption [25,39]. As a result, the nucleation rate is enhanced according to Gibbs equation and energy barrier for nucleation described below. The Gibbs equation is expressed by:

$$d\gamma = - \sum_i \Gamma_i d\mu_i \quad (1)$$

where γ , Γ_i and μ_i represent the surface tension, the superficial adsorption concentration and chemical potential of the adsorbed species i [41], respectively. The nucleation energy barrier ΔG_{crit} is expressed by:

$$\Delta G_{\text{crit}} = \frac{16\pi}{3} \frac{\gamma^3 V_m^2}{(RT \ln S)^2} \quad (2)$$

where R , T , S and V_m are universal gas constant, temperature, the supersaturation and the molar volume of monomers [41], respectively. Based on Equations (1) and (2), the adsorption of the surfactant molecules reduces the surface tension, which further lowers the nucleation energy barrier and enhances the nucleation rate. At the same time, the surfactants molecules adsorbed on the surfaces of the WO_{3-x} nuclei form the surfactant layers to prevent their aggregation and growth. After these nuclei experience quenching in the solution, they are formed into irregular crystal nanodots (CNDs) with a small size, which are evidenced by the TEM results. Here, we should note that the size refers to the size of the WO_{3-x} CNDs without the surfactant layers. Due to the attachment of the surfactant layers on the WO_{3-x} CNDs, the size of the WO_{3-x} CNDs becomes relatively large due to the long carbon chain of the surfactant molecules. In addition, the surfactants result in the increase in the viscosity η of the solution, which can be addressed by the early studies [42]. In Ref. [42], the results indicate that the viscosity of a mixture composed of an organic compound with high viscosity (e.g., ethanol, butanol or octanol) and another organic compound with low viscosity (e.g., propylamine) reduces with the increase in the mole fraction of the compound with low viscosity. In other words, the viscosity of

the mixtures increases with the increase in the mole fraction of the compound with high viscosity. Due to the relation of mole fraction x with volume v ($x = \rho v / M$, where ρ and M are the density and molar mass), the viscosity of the mixtures increases with the increase in the volume of the compound with high viscosity. The viscosity of acetic, butyric and oleic acids at 20 °C is 1.23, 1.54 and 34.8 mPa·s [43,44], respectively. According to these data, the viscosity of the solutions increases with the increase in the volume of the surfactants. Therefore, the introduction of the surfactant leads to the change in the motion of the WO_{3-x} CNDs. The relation of diffusion coefficient D_{diff} with the radius of particle r and viscosity η is:

$$D_{\text{diff}} = \frac{k_B T}{6\pi r \eta} \quad (3)$$

where k_B is Boltzmann's constant [22]. According to Equation (3), the diffusion coefficient is reversely proportional to the radius of particle and the viscosity of solution. Therefore, the motion of the WO_{3-x} CNDs becomes slow in the solution. In other words, the aggregation of the WO_{3-x} CNDs takes place in the interior of the solution. Because the formation of the WO_{3-x} CNDs originates from the $\text{WCl}_6 - \text{CH}_3\text{COO}$ reaction, the slow speed of the WO_{3-x} CNDs makes them located in the reaction region, i.e., their distribution in the solution is nonuniform.

2. Aggregation of WO_{3-x} nanoparticles

Unlike the aggregation of the WO_{3-x} NCs in acetic acid, the WO_{3-x} CNDs are aggregated into the submicro-spherical-like, submicro-spherical and micro-spherical structures under the surfactants (Figure 5), which are related to the repulsion interactions between the WO_{3-x} CNDs and the property of solution. In this section, the aggregation under the surfactants is analyzed.

For the convenience of analysis, the WO_{3-x} CNDs are considered to be a spherical structure and the surfactant molecule is represented by a bending line, which are presented in Figure 9. Due to Brownian motion, the surfactant layers are overlapped when two WO_{3-x} CND approach. As a result, the increased concentration of the surfactant tails in the overlap region increases osmotic pressure, generating steric repulsion [25,45]. The theoretical studies indicate the osmotic potential V_{Osm} is related to the thickness of the polymer layer and the volume fraction of polymer molecules in the layer [46], which is expressed by:

$$V_{\text{Osm}} = 0, \quad d \geq 2l \quad (4)$$

$$V_{\text{Osm}} = k_B T \frac{4\pi a}{v_1} \varnothing_p^2 \left(\frac{1}{2} - \chi \right) \left(l - \frac{d}{2} \right)^2, \quad l \leq d < 2l \quad (5)$$

$$V_{\text{Osm}} = k_B T \frac{4\pi a}{v_1} \varnothing_p^2 \left(\frac{1}{2} - \chi \right) l^2 \left(\frac{d}{2l} - \frac{1}{4} - \ln \left(\frac{d}{l} \right) \right), \quad d < l \quad (6)$$

where a , l , d and \varnothing_p represent the radius of a particle, the thickness of polymer layer, the distance between the particles and the effective volume fraction of polymer molecules in the polymer layer, respectively, and v_1 and χ correspond to the volume of one solvent molecule and the Flory–Huggins solvency parameter, respectively. Here, \varnothing_p depends on the concentration of surfactant tails in the overlap region of the surfactant layers [25]. Form Equations (5) and (6), we obtain:

$$\frac{\partial V_{\text{Osm}}}{\partial (l/d)} = 2k_B T \frac{4\pi a}{v_1} \varnothing_p^2 d^2 \left(\frac{1}{2} - \chi \right) \left(\frac{l}{d} - \frac{1}{2} \right) > 0, \quad l \leq d < 2l \quad (7)$$

$$\frac{\partial V_{\text{Osm}}}{\partial (d/l)} = k_B T \frac{4\pi a}{v_1} \varnothing_p^2 \left(\frac{1}{2} - \chi \right) l^2 \left(\frac{1}{2} - \frac{l}{d} \right) < 0, \quad d < l \quad (8)$$

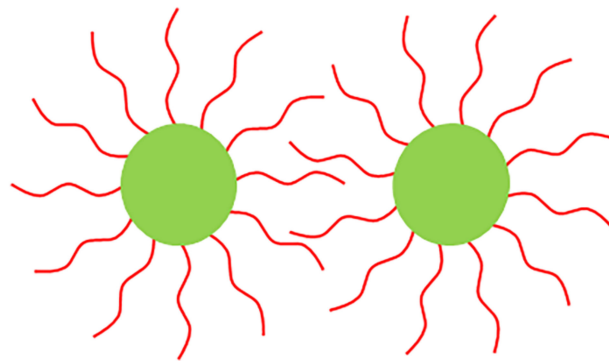


Figure 9. Schematic diagram of steric repulsion produced by the surfactant layers on the WO_{3-x} CNDs. Adapted with modification from Refs. [25,45].

According to Equations (7) and (8), the steric repulsion increases with the thickness of the surfactant layers and the number of the surfactant tails in the overlap region. If the surfactant layers are thin, the steric repulsion is increased by increasing the amount of the surfactants.

In the initial process of aggregation, the distribution of the WO_{3-x} CNDs in the reaction region is nonuniform. Due to long chains of the surfactant molecules, the diffusion is slow. As a result, a number of the WO_{3-x} CNDs are partly covered by the surfactant molecules and others are completely capped, which are shown in Figure 10a. Under the attraction interactions, the WO_{3-x} CNDs are aggregated in an irregular structure (Figure 10a). With the progress of aggregation, the surfactant molecules gradually come into the irregular structure through diffusion and are adsorbed on the WO_{3-x} CNDs (Figure 10b). As shown in Figure 10b, the concentration of the surfactant tails around the WO_{3-x} CNDs increases, which leads to the enhancement of the steric repulsion [25]. In this situation, the attraction interactions between the WO_{3-x} CNDs are gradually weakened to tune the aggregation process. If the steric repulsion cannot balance the attraction interactions, the WO_{3-x} CNDs are aggregated, but the arrangement of the WO_{3-x} CNDs is tuned due to the presence of the steric repulsion (Figure 10b). Depending on the steric repulsion, different WO_{3-x} CNDs form the submicro-spherical-like or submicro-spherical and micro-spherical structures to reduce the surface energy, which are shown in Figure 10b,c.

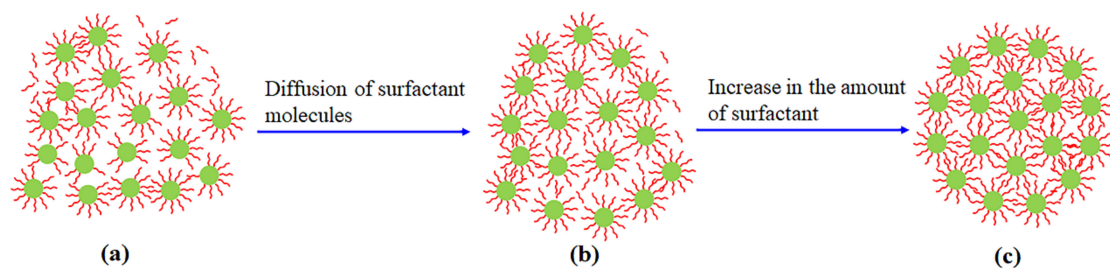


Figure 10. Aggregation schematic of spherical-like and spherical WO_{3-x} aggregates. (a) irregular structure; (b) submicro-spherical-like structure; (c) submicro- or micro-spherical structure.

Due to the short chain of the butyric acid molecule (~ 0.6 nm) compared to an oleic acid molecule (~ 2.5 nm) [10], the butyric acid molecules form thin surfactant layers on the WO_{3-x} CNDs. With the increase in the amount of butyric acid, the steric repulsion is enhanced. As a result, the aggregation is further tuned and the structure converts from the submicro-spherical-like to submicro-spherical shapes (Figure 10b,c). These are the reasons why Figure 5b,c present the submicro-spherical-like and submicro-spherical WO_{3-x} aggregates. For oleic acid, the long chain of molecules results in the formation of the thick surfactant layers on the WO_{3-x} CNDs, which generates a strong steric repulsion [47]. Furthermore, the separation between the WO_{3-x} CNDs is increased. Consequently, the

WO_{3-x} CNDs are easily rearranged in a large region to form the micro-spherical structure. Therefore, Figure 5d shows the spherical structure with a micron size.

With the increase in the amount of oleic acid in the solution, the viscosity of the solution is enhanced, which leads to a low diffusion speed of the oleic molecules. As a result, there are a small number of the oleic acid molecules to adsorb on the WO_{3-x} CNDs. When both the WO_{3-x} NPs approach, there are few of the oleic tails between the WO_{3-x} CNDs. Based on Equation (5), the steric repulsion is weak, which results in the aggregation of the WO_{3-x} CNDs. Simultaneously, some oleic acid molecules adsorbed on the WO_{3-x} NPs are deformed by compression during the aggregation [5]. This further shortens the separation between the WO_{3-x} NPs and improves the attraction interactions. In this case, the WO_{3-x} CNDs are aggregated into the submicro-spherical-like structure, which is confirmed by Figure 5e.

3.5. PL Property

The PL spectra presented in Figure 11 address the PL properties of the as-synthesized WO_{3-x} aggregates. From Figure 11a, one can see that the PL emission from samples B–E exhibits the PL quenching. To confirm the PL bands, a Labspec 5 software was used to fit the PL spectra of samples A, B and D after linear background subtraction. Figure 11a indicates that the PL spectra of samples C and E are similar to the PL spectra of samples B and D, respectively. Here, the PL spectra of samples A, B and D as the typical PL spectra are fitted. The fitted PL peaks are respectively presented in Figure 11b–d, which indicate that the as-synthesized WO_{3-x} aggregates emit ultraviolet (UV), blue, green, red and near-infrared (NIR) light.

In the early work [22], the studies on the PL emission from the WO_{3-x} nanomaterials indicate that the PL emission is related to the band–band transition and the defect level–level transition. The oxygen vacancies in the WO_{3-x} materials form three defect states including the neutral (V_O^0), single charged (V_O^+) and doubly charged (V_O^{2+}) states [16]. In the electronic structure, the V_O^0 and V_O^{2+} states form the resonant state levels in the valence and conduction bands, and the V_O^+ state form a level in the bandgap [16]. Therefore, different transitions give rise to different PL emissions.

According to the early studies [22], the UV emission (384–389 nm) is attributed to the recombination between the electron occupying the resonant defect state in the conduction band and the hole in the valence band, and the blue emission (420–433 nm) can be attributed to the band–band transition. For the transitions related to defect levels, the transition from V_O^+ to V_O^0 leads to the green emission (566–576 nm) and the transitions from V_O^{2+} to V_O^+ and V_O^{2+} to V_O^0 generate the red emission (625 and 632 nm), respectively. The green emission (504–512 nm) is related to the $(V_O^0)^* \rightarrow V_O^+$ transition (where * represents the nonrelaxed state). The NIR PL emission (749–753 nm) originates from the relaxation of polarons caused by the coupling of lattice distortion with carries [13].

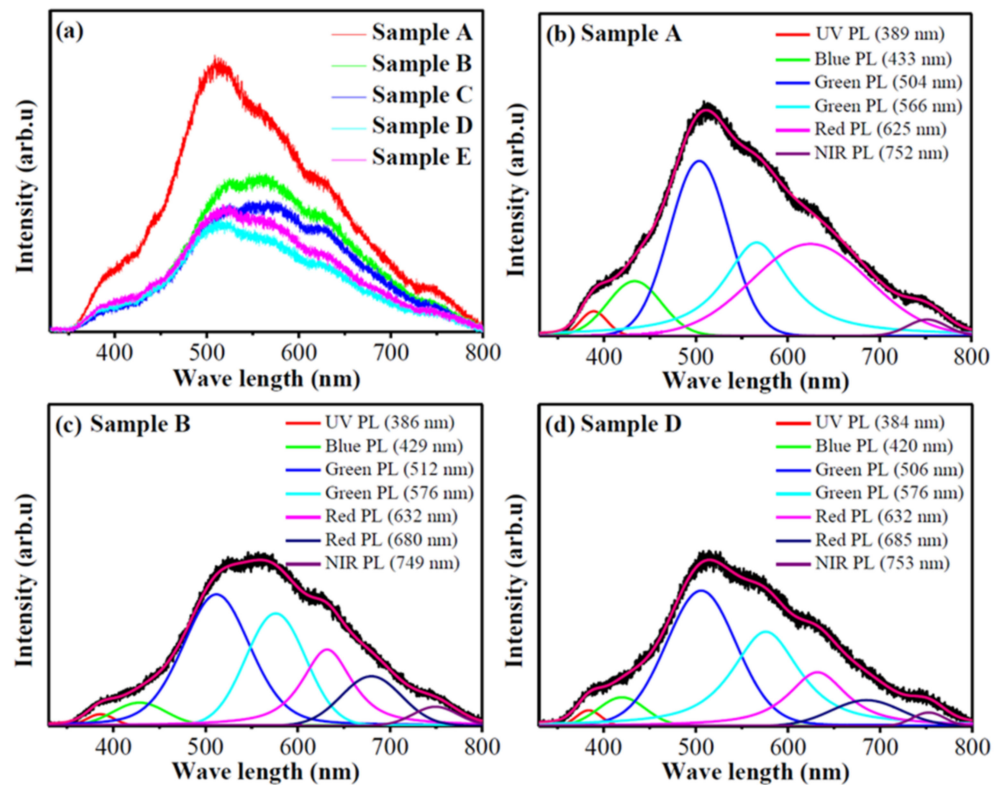


Figure 11. (a) PL spectra of samples A–E and (b–d) deconvoluted PL peaks for the PL spectra of samples A, B and D. The data in the images (b–d) correspond to the wave lengths of PL emissions.

Compared with Figure 11b, Figure 11c,d exhibit new PL bands at ~ 680 and 685 nm, which may be related to the coupling between the WO_{3-x} CNDs [5]. The aggregation indicates the occurrence of the coupling between the neighboring WO_{3-x} CNDs depending on their separation. In the solution containing the surfactant, the short carbon chain (~ 0.6 nm) of the butyric acid molecule easily causes the coupling between the WO_{3-x} CNDs [5,10]. For the oleic acid molecules, the long carbon chain (~ 2.5 nm) should prevent the coupling [10]. However, their deformation reduces the separation between the WO_{3-x} CNDs [5]. As a result, coupling can occur between the WO_{3-x} CNDs. The coupling can form a new level in the bandgap of the WO_{3-x} materials [5], which generates the PL emission at about 680 and 685 nm.

The PL quenching shown in Figure 11a can originate from the coupling between the WO_{3-x} CNDs and the trapping centers arising from the surfactant molecules. Due to the coupling between the WO_{3-x} CNDs, the charge transfer occurs between the WO_{3-x} CNDs [5], which reduces the recombination probability of the photogenerated electrons and holes to decrease the PL emission. The XPS results indicate that the carboxylic acid molecules coordinate with the WO_{3-x} CNDs in bidentate mode. The bidentate structure can trap the photogenerated electrons to quench PL emission [48]. When the PL emission was measured, the irradiation of laser results in the desorption of the residual acetic acid molecules due to small molecular weight, while the butyric and oleic acid molecules are not easily desorbed. As a result, the trapping centers in sample A are reduced and sample A generates strong PL emission (see Figure 11a). Compared with the PL spectra of samples B and D in Figure 11a, the PL intensity of sample D is weaker than that of sample B. This may be related to their aggregation. From Figure 5, one can see that sample D is composed of the micro-spheres, which imply that there are a number of trapping centers. Thus, Figure 11a shows that the PL emission from sample D is weak compared to sample B. Figure 5c,e indicate that there is a small difference in the morphologies of samples C and E, i.e., they may have almost the same amount of trapping centers. Therefore, the PL intensity of sample C is almost the same as that of sample E.

4. Conclusions

In summary, the WO_{3-x} materials with different structures were synthesized under the butyric or oleic acid surfactants. The results indicate that the WO_{3-x} CNs can be aggregated into the submicro-spherical-like, submicro-spherical or micro-spherical aggregates depending on the steric repulsion of butyric acid or oleic acid, which are related to their amount employed in the process of syntheses. In other words, the increase in the amount of butyric acid leads to the conversion of submicro-spherical-like to submicro-spherical WO_{3-x} aggregates, while the increased oleic acid causes the change in the micro-spherical to submicro-spherical-like conversion of the WO_{3-x} aggregates. Based on the analyses on the osmotic potential of polymers, the structural conversion of WO_{3-x} aggregates originates from the change in the steric repulsion caused by the surfactant layers, the adsorption and deformation of surfactant molecules on the WO_{3-x} CNs. Furthermore, the PL properties of the WO_{3-x} aggregates were studied. The WO_{3-x} aggregates generate the UV, blue, green, red and NIR PL emission, which are related to the inter-band transition and defect level-associated transition as well as the relaxation of polarons caused by the coupling of lattice distortion with carries. The PL quenching of the submicro-spherical-like, submicro-spherical and micro-spherical WO_{3-x} aggregates are associated with the coupling between the WO_{3-x} CNs and the trapping centers originating from the surfactant molecules on the WO_{3-x} CNs. Our achievements can effectively tune the structure of WO_3 -based nanomaterials and contribute to the development of next-generation optoelectronic nanodevices.

Author Contributions: Conceptualization, B.W.; Investigation, B.W., X.Z., H.X., Y.Z., U.C. and K.O.; Writing—original draft, B.W.; Writing—review and editing, X.Z., H.X., Y.Z., U.C. and K.O. All authors have read and agreed to the published version of the manuscript.

Funding: This research was funded by the National Natural Science Foundation of China (Grant No. 12175141); Natural Science Foundation of Shanghai (Grant No. 21ZR1435200); National Key Research and Development Program of China (Grant No. 2018YFA0306304); Australian Research Council and QUT Centre for Materials Science; Slovenia-China Bilateral grant BI-CN; and Slovenian Research Agency (ARRS) grant N2-0091.

Data Availability Statement: Not applicable.

Conflicts of Interest: The authors declare no conflict of interest.

References

1. Pan, D.; Fang, Z.; Yang, E.; Ning, Z.; Zhou, Q.; Chen, K.; Zheng, Y.; Zhang, Y.; Shen, Y. Facile preparation of WO_{3-x} dots with remarkably low toxicity and uncompromised activity as coreactants for clinic electrochemiluminescent diagnosis. *Angew. Chem. Int. Ed.* **2020**, *59*, 16747–16754. [[CrossRef](#)] [[PubMed](#)]
2. Han, X.; Li, X.; Wang, R.; Liu, J.; Liu, L. Study on the gamma irradiation characteristics of a carbon nanotube sponge/polydimethylsiloxane/tungsten oxide flexible force-sensitive structure. *Micromachines* **2022**, *13*, 1024. [[CrossRef](#)] [[PubMed](#)]
3. Hou, K.; Han, J.; Tang, Z. Formation of supraparticles and their application in catalysis. *ACS Mater. Lett.* **2020**, *2*, 95–106. [[CrossRef](#)]
4. Zhao, Q.; Gouget, G.; Guo, J.; Yang, S.; Zhao, T.; Straus, D.B.; Qian, C.; Oh, N.; Wang, H.; Murray, C.B.; et al. Enhanced carrier transport in strongly coupled, epitaxially fused CdSe nanocrystal solids. *Nano Lett.* **2021**, *21*, 3318–3324. [[CrossRef](#)] [[PubMed](#)]
5. Luo, D.; Qin, X.; Song, Q.; Qiao, X.; Zhang, Z.; Xue, Z.; Liu, C.; Mo, G.; Wang, T. Ordered superparticles with an enhanced photoelectric effect by sub-nanometer interparticle distance. *Adv. Funct. Mater.* **2017**, *27*, 1701982. [[CrossRef](#)]
6. Narayanaswamy, A.; Xu, H.; Pradhan, N.; Peng, X. Crystalline nanoflowers with different chemical compositions and physical properties grown by limited ligand protection. *Angew. Chem.* **2006**, *118*, 5487–5490. [[CrossRef](#)]
7. Evers, W.H.; Schins, J.M.; Aerts, M.; Kulkarni, A.; Capiod, P.; Berthe, M.; Grandidier, B.; Delerue, C.; van der Zant, H.S.J.; van Overbeek, C.; et al. High charge mobility in two-dimensional percolative networks of PbSe quantum dots connected by atomic bonds. *Nat. Commun.* **2015**, *6*, 8195. [[CrossRef](#)]
8. Pereira, R.N.; Coutinho, J.; Niesar, S.; Oliveira, T.A.; Aigner, W.; Wiggers, H.; Rayson, M.J.; Briddon, P.; Brandt, M.S.; Stutzmann, M. Resonant electronic coupling enabled by small molecules in nanocrystal solids. *Nano Lett.* **2014**, *14*, 3817–3826. [[CrossRef](#)]
9. Liu, Y.; Gibbs, M.; Puthussery, J.; Gaik, S.; Ihly, R.; Hillhouse, H.W.; Law, M. Dependence of carrier mobility on nanocrystal size and ligand length in PbSe nanocrystal solids. *Nano Lett.* **2010**, *10*, 1960–1969. [[CrossRef](#)]
10. Konstantatos, G.; Howard, I.; Fischer, A.; Hoogland, S.; Clifford, J.; Klem, E.; Levina, L.; Sargent, E.H. Ultrasensitive solution-cast quantum dot photodetectors. *Nature* **2006**, *442*, 180–183. [[CrossRef](#)]

11. Tang, Z.; Kotov, N.A.; Giersig, M. Spontaneous organization of single CdTe nanoparticles into luminescent nanowires. *Science* **2002**, *297*, 237–240. [[CrossRef](#)]
12. Johansson, M.B.; Zietz, B.; Niklasson, G.A.; Österlund, L. Optical properties of nanocrystalline WO₃ and WO_{3-x} thin films prepared by DC magnetron sputtering. *J. Appl. Phys.* **2014**, *115*, 213510. [[CrossRef](#)]
13. Wang, B.B.; Zhong, X.X.; He, C.L.; Zhang, B.; Cvelbar, U.; Ostrikov, K. Solvent-dependent structures and photoluminescence of WO_{3-x} nanomaterials grown in nonaqueous solutions. *J. Alloys Compd.* **2021**, *854*, 157249. [[CrossRef](#)]
14. Paik, T.; Cargnello, M.; Gordon, T.R.; Zhang, S.; Yun, H.; Lee, J.D.; Woo, H.Y.; Oh, S.J.; Kagan, C.R.; Fornasiero, P.; et al. Photocatalytic hydrogen evolution from substoichiometric colloidal WO_{3-x} nanowires. *ACS Energy Lett.* **2018**, *3*, 1904–1910. [[CrossRef](#)]
15. Chen, J.; Yu, D.; Liao, W.; Zheng, M.; Xiao, L.; Zhu, H.; Zhang, M.; Du, M.; Yao, J. WO_{3-x} nanoplates grown on carbon nanofibers for an efficient electrocatalytic hydrogen evolution reaction. *ACS Appl. Mater. Interfaces* **2016**, *8*, 18132–18139. [[CrossRef](#)]
16. Deb, S.K. Opportunities and challenges in science and technology of WO₃ for electrochromic and related applications. *Sol. Energy Mater. Sol. Cells* **2008**, *92*, 245–258. [[CrossRef](#)]
17. Wang, F.; Valentin, C.D.; Pacchioni, G. Semiconductor-to-metal transition in WO_{3-x}: Nature of the oxygen vacancy. *Phys. Rev. B* **2011**, *84*, 073103. [[CrossRef](#)]
18. Gerosa, M.; Valentin, C.D.; Onida, G.; Bottani, C.E.; Pacchioni, G. Anisotropic effects of oxygen vacancies on electrochromic properties and conductivity of γ -monoclinic WO₃. *J. Phys. Chem. C* **2016**, *120*, 11716–11726. [[CrossRef](#)]
19. Xiao, X.; Zhou, X.; Ma, J.; Zhu, Y.; Cheng, X.; Luo, W.; Deng, Y. Rational synthesis and gas sensing performance of ordered mesoporous semiconducting WO₃/NiO composites. *ACS Appl. Mater. Interfaces* **2019**, *11*, 26268–26276. [[CrossRef](#)]
20. Duan, G.; Chen, L.; Jing, Z.; Luna, P.D.; Wen, L.; Zhang, L.; Zhao, L.; Xu, J.; Li, Z.; Yang, Z.; et al. Robust antibacterial activity of tungsten oxide (WO_{3-x}) nanodots. *Chem. Res. Toxicol.* **2019**, *32*, 1357–1366. [[CrossRef](#)]
21. Wang, B.B.; Zhong, X.X.; He, C.L.; Zhang, B.; Shao, R.W.; Shvalya, V.; Cvelbar, U.; Ostrikov, K. Controlling oxygen vacancies of WO_x suboxides by ZnWO₄ nanophase hybridization. *Mater. Sci. Eng. B* **2020**, *262*, 114706. [[CrossRef](#)]
22. Wang, B.B.; Zhong, X.X.; He, C.L.; Zhang, B.; Cvelbar, U.; Ostrikov, K. Nanostructure conversion and enhanced photoluminescence of vacancy engineered substoichiometric tungsten oxide nanomaterials. *Mater. Chem. Phys.* **2021**, *262*, 124311. [[CrossRef](#)]
23. Wang, B.B.; Zhong, X.X.; Zhu, J.; Zhang, Y.; Cvelbar, U.; Ostrikov, K. Single-step synthesis of sub-stoichiometric tungsten oxide particles in mixed acetic and oleic acids: Structural conversion and photoluminescence enhancement. *J. Alloys Compd.* **2022**, *899*, 163265. [[CrossRef](#)]
24. Wang, B.; Zhong, X.; Zhang, Y.; Xu, H.; Zhang, Y. Microspheres assembled by WO_{3-x} nanoparticles under action of dual surfactants: Structure and photoluminescence properties. *Opt. Mater.* **2022**, *129*, 112550. [[CrossRef](#)]
25. Piacenza, E.; Presentato, A.; Turner, R.J. Stability of biogenic metal(loid) nanomaterials related to the colloidal stabilization theory of chemical nanostructures. *Crit. Rev. Biotechnol.* **2018**, *38*, 1137–1156. [[CrossRef](#)]
26. Fulton, G.; Lunev, A. Probing the correlation between phase evolution and growth kinetics in the oxide layers of tungsten using Raman spectroscopy and EBSD. *Corros. Sci.* **2020**, *162*, 108221. [[CrossRef](#)]
27. Daniel, M.F.; Desbat, B.; Lassegues, J.C. Infrared and Raman study of WO₃ tungsten trioxides and WO₃·xH₂O tungsten trioxide hydrates. *J. Solid State Chem.* **1987**, *67*, 235–247. [[CrossRef](#)]
28. Garcia-Sanchez, R.F.; Ahmido, T.; Casimir, D.; Baliga, S.; Misra, P. Thermal effects associated with the Raman spectroscopy of WO₃ gas-sensor materials. *J. Phys. Chem. A* **2013**, *117*, 13825–13831. [[CrossRef](#)]
29. Blackman, C.S.; Parkin, I.P. Atmospheric pressure chemical vapor deposition of crystalline monoclinic WO₃ and WO_{3-x} thin films from reaction of WCl₆ with O-containing solvents and their photochromic and electrochromic properties. *Chem. Mater.* **2005**, *17*, 1583–1590. [[CrossRef](#)]
30. Yu, W.; Shen, Z.; Peng, F.; Lu, Y.; Ge, M.; Fu, X.; Sun, Y.; Chen, X.; Dai, N. Improving gas sensing performance by oxygen vacancies in sub-stoichiometric WO_{3-x}. *RSC Adv.* **2019**, *9*, 7723–7728. [[CrossRef](#)]
31. Wagner, C.D.; Riggs, W.M.; Davis, L.E.; Moulder, J.F.; Muilenberg, G.E. *Handbook of X-ray Photoelectron Spectroscopy*; Perkin-Elmer Corp., Physical Electronics Division: Eden Prairie, MI, USA, 1979; Volume 38, pp. 147–184.
32. He, Y.; Liang, A.; Zhu, D.; Hu, M.; Xu, L.; Chao, S.; Zhou, W.; Wu, Y.; Xu, J.; Zhao, F. Organic-inorganic hybrid electrode engineering for high-performance asymmetric supercapacitor based on WO₃-CeO₂ nanowires with oxygen vacancies. *Appl. Surf. Sci.* **2022**, *573*, 151624. [[CrossRef](#)]
33. Zhang, N.; Li, F.; Yin, Y.; Han, J.; Li, X.; Liu, C.; Zhou, J.; Wen, S.; Adimi, S.; Chen, Y.; et al. Gas sensor based on TiO₂ nanofibers decorated with monodispersed WO₃ nanocubes for fast and selective xylene detection. *Mater. Sci. Eng. B* **2021**, *263*, 114901. [[CrossRef](#)]
34. Wilson, D.; Langell, M.A. XPS analysis of oleylamine/oleic acid capped Fe₃O₄ nanoparticles as a function of temperature. *Appl. Surf. Sci.* **2014**, *303*, 6–13. [[CrossRef](#)]
35. Mahdavi, M.; Ahmad, M.B.; Haron, M.J.; Namvar, F.; Nadi, B.; Rahman, M.Z.A.; Amin, J. Synthesis, surface modification and characterisation of biocompatible magnetic iron oxide nanoparticles for biomedical applications. *Molecules* **2013**, *18*, 7533–7548. [[CrossRef](#)]
36. Chen, S.-H.; Yu, C.-F.; Wang, C.-J.; Chen, S.-H.; Chen, Y.-D.; Chen, T.-C.; Lin, C.-F. Light enhancement of plasmonic nano-structure for PLEDs at RGB wavelengths. *Org. Electron.* **2016**, *38*, 337–343. [[CrossRef](#)]

37. Chen, S.-H.; Hsu, P.-J. Luminous efficiency improvement of polymer light-emitting diodes with platinum nanolayer at the PEDOT:PSS-ITO interface. *Opt. Lett.* **2021**, *46*, 6039–6042. [[CrossRef](#)]
38. Segets, D.; Marczak, R.; Schäfer, S.; Paula, C.; Gnichwitz, J.-F.; Hirsch, A.; Peukert, W. Experimental and theoretical studies of the colloidal stability of nanoparticles—A general interpretation based on stability maps. *ACS Nano* **2011**, *5*, 4658–4669. [[CrossRef](#)]
39. Hotze, E.M.; Phenrat, T.; Lowry, G.V. Nanoparticle aggregation: Challenges to understanding transport and reactivity in the environment. *J. Environ. Qual.* **2010**, *39*, 1909–1924. [[CrossRef](#)]
40. Patil, V.B.; Adhyapak, P.V.; Suryavanshi, S.S.; Mulla, I.S. Oxalic acid induced hydrothermal synthesis of single crystalline tungsten oxide nanorods. *J. Alloys Compd.* **2014**, *590*, 283–288. [[CrossRef](#)]
41. Vayssieres, L. On the design of advanced metal oxide nanomaterials. *Int. J. Nanotechnol.* **2004**, *1*, 1–41. [[CrossRef](#)]
42. Oswal, S.L.; Desai, H.S. Studies of viscosity and excess molar volume of binary mixtures. 1. Propylamineq1-alkanol mixtures at 303.15 and 313.15 K. *Fluid Phase Equilibria* **1998**, *149*, 359–376. [[CrossRef](#)]
43. Shen, Y.; Liu, M. Viscosity of organic compounds. *J. South-Cent. Coll. Natl. (Nat. Sci.)* **1997**, *16*, 5–10. (In Chinese)
44. Sagdeev, D.; Gabitov, I.; Isyanov, C.; Khairutdinov, V.; Farakhov, M.; Zaripov, Z.; Abdulagatov, I. Densities and viscosities of oleic acid at atmospheric pressure. *J. Am. Oil Chem. Soc.* **2019**, *96*, 647–662. [[CrossRef](#)]
45. Johes, R.A.L. *Soft Condensed Matter*; Oxford University Press: Oxford, England, 2002; p. 60.
46. Fritz, G.; Schädler, V.; Willenbacher, N.; Wagner, N.J. Electrosteric stabilization of colloidal dispersions. *Langmuir* **2002**, *18*, 6381–6390. [[CrossRef](#)]
47. Kotov, N.K. Practical aspects of self-organization of nanoparticles: Experimental guide and future applications. *J. Mater. Chem.* **2011**, *21*, 16673–16674. [[CrossRef](#)]
48. Sakohara, S.; Tickanen, L.D.; Anderson, M.A. Luminescence properties of thin zinc oxide membranes prepared by the Sol-Gel technique: Change in visible luminescence during firing. *J. Phys. Chem.* **1992**, *96*, 11086–11091. [[CrossRef](#)]